Synergistic enhancement of photocatalytic CO_2 reduction by plasmonic Au nanoparticles on TiO_2 decorated N-graphene heterostructure catalyst for high selectivity methane production

Khaja Mohaideen Kamal [a,*], Rekha Narayan [b], Narendraraj Chandran [c], Stefan Popović [b], Mohammed Azeezulla Nazrulla [b], Janez Kovač [d], Nika Vrtovec [f], Marjan Bele [b], Nejc Hodnik [b], Marjeta Maček Kržmanc [e], Blaž Likozar [a,*]

[a] *Department of Catalysis and Chemical Reaction Engineering, National Institute of Chemistry, 1001 Ljubljana, Slovenia*
[b] *Department of Materials Chemistry, National Institute of Chemistry, 1001 Ljubljana, Slovenia*
[c] *Tescan Brno S.R.O, Libušina třída 1, 623 00 Brno, Czech Republic*
[d] *Department for Surface Engineering, Jozef Stefan Institute, 1000 Ljubljana, Slovenia*
[e] *Advanced Materials Department, Jožef Stefan Institute, 1000 Ljubljana, Slovenia*
[f] *Department of Inorganic Chemistry and Technology, National Institute of Chemistry, 1001 Ljubljana, Slovenia. Faculty of Chemistry and Chemical Technology, University of Ljubljana, Večna pot 113, 1000 Ljubljana, Slovenia*

ARTICLE INFO

ABSTRACT

Energy-efficient photocatalytic CO_2 reduction (PCO$_2$R) into sustainable solar fuels is a highly enticing challenge for simultaneous settling of energy and environmental issues. Herein, we illustrate the synthesis and photocatalytic performance of a judiciously designed plasmonic Au nanoparticles photodeposited on TiO_2-decorated N-doped graphene (ANGT-*x*) heterostructure catalyst showing remarkably enhanced CO_2 reduction activity with high selectivity for methane production. Compared to typical binary Au-TiO_2 photocatalyst, the ANGT2 exhibited almost 60 times higher electron consumption rate ($R_{electron}$) value $\sim$ 742.39 μmol g^{-1}h^{-1} for the reduced products, which, to the best of our knowledge is the highest PCO$_2$R rate ever reported under comparable conditions. The superior performance of ANGT2 catalyst is attributed to the synergistic contributions from improved light absorbance, enhanced CO_2 uptake together with improved charge transfer kinetics and efficient suppression of photogenerated (e-h) recombination rate bestowed by seamless interfacial contact between Au NPs and N-graphene-TiO_2 components.

1. Introduction

Rising concentration of anthropogenic carbon dioxide (CO_2) gas in the atmosphere is one key reason for global warming and climate change.[1–6] Reducing the amount of CO_2 in the atmosphere by utilizing it for sustainable energy or fuel production can solve the two global issues of energy shortage and environmental pollution in one shot. Towards this goal photocatalytic CO_2 reduction (PCO$_2$R) to hydrocarbon solar fuels (CO, CH_4, C_2H_2, C_2H_4, C_2H_6 etc.) using the inexhaustible solar energy (the so-called artificial photosynthesis) has emerged as a highly promising environment benign approach.[7–9] Recently 2D nanostructures, especially graphene hybridized materials have garnered tremendous research interest in PCO$_2$R majorly because

graphene can act as a potential electron sink and transport bridge due to its intrinsic high electron mobility.[10] Owing to its unique 2D large π-conjugated structure, graphene when integrated with photoactive material can act as excellent catalyst support with high surface area promoting the uniform distribution and prevent aggregation of nanostructured photoactive components. Thus, coupling of graphene with semiconductors mainly titanium dioxide (TiO_2) has been widely used in PCO$_2$R because it extends the optical absorption of TiO_2 to visible region and reduces the diffusion path length of photogenerated charge carriers. [11] However, the overall efficiency of most graphene-based composites reported till date in PCO$_2$R remains unsatisfactory. Studies show that graphene derivatives with high defect density and large sheet resistance, such reduced graphene oxide (rGO) have unfavorable influence on the

---

photoelectron separation and transfer.[12] Extraordinarily, nitrogen-doped graphene (NG), is getting more and more attention to construct high-performance photocatalytic system over pristine graphene.[13] N-doping in graphene networks is capable to facilitate the formation of activated regions where the N-atoms are adjacent to the carbon atoms and promote the photocatalyst to host guest reactive species due to the high charge and spin densities of N-atoms.[14,15] The N-sites can be adsorption centers to anchor and activate CO_2 molecules, and directly participate in catalytic reactions.[16] N-atoms can also act as binding sites to coordinate with metal ions, which promote the intimate contact between photocatalyst and graphitic matrix, thereby enhance the photocatalytic activity of graphene-based materials. As a result, many research studies have sparked on the integrating photocatalysts with NG.[17–19] For instance, Yu's group reported a novel in-situ grown monolayer NG on CdS, showing reasonable PCO_2R.[18] Enhanced photocatalytic activity for H_2 generation under visible-light irradiation was reported by Cheng and co-workers using TiO_2 nanoparticles functionalized NG.[19] It is noteworthy that most of these NG-based photocatalysts are limited to binary composite systems, which is the still far from reaching the expected capability of the composites system. Hence, there is still plenty of room for further improvement in the performance of NG-based photocatalysts. Constructing ternary hybrid structures incorporating high quality and excellent electrical conductivity NG-based photocatalysts derivative in combination with other suitable active ingredients favorable for high-efficiency PCO_2R appear attractive strategy. Attaching noble-metal (Au, Ag, Pd, Pt) nanoparticles co-catalysts over semiconductors is yet another promising approach that has shown superior PCO_2R activity due to their localized surface plasmon resonance (LSPR) extending the visible light absorption and improving charge separation.[20–23] To date, numerous thermal- and photo-induced catalytic reactions were discovered on titanate-supported gold catalysts. The mechanisms of CO_2 hydrogenation are quite different in thermal and photo generated reactions. However, the thermal induced CO_2 hydrogenation on 1D and 3D titania-like catalysts exclusively produce CO as a sole product.[24–27] The unique coupling of high photoactivity TiO_2 with LSPR effect of Au NPs and excellent electronic transport plus CO_2 adsorption properties of N-doped graphene promise high photocatalytic efficiency. However, till now very few ternary hybrid photocatalysts based on N-doped graphitic structures have been reported, but to the best of our knowledge none specifically for PCO_2R.[28].

Herein, we constructed a ternary heterostructure photocatalyst comprising N-doped graphene, titanium dioxide (TiO_2) and gold nanoparticles (Au NPs), namely Au-TiO_2 decorated N-doped graphene (ANGT) and demonstrated its high efficiency for PCO_2R under visible light. Furthermore, this kind of distinctive ternary ANGT photocatalytic system has greatly overcome the drawbacks compared with the single/binary component catalysts and realized extended visible light response, high surface adsorption of CO_2, high rate of photogenerated electron-hole (e-h) transport, low rate of photogenerated (e-h) recombination, high selectivity for specific hydrocarbon (C1 and C2) products and long-term stability. Mechanism toward the photocatalysis process of such the ternary system has been proposed supported by theoretical DFT calculations and discussed in detail. Notably, this work exhibits new strategy to achieve enhanced solar photocatalytic activity and provides new insights for the design and development of high-performance ternary heterostructure photocatalysts.

2. Experimental

2.1. Materials

All reagents were analytical grade and used without any further purification. Milli-Q water was used throughout this work.

2.2. Preparation of N-doped graphene (NG)

Starting material graphene oxide (GO) was prepared from graphite flakes (Aldrich) by using a modified Hummer's oxidation process and then GO was annealed in NH_3 atmosphere to obtain N-graphene materials. Briefly, GO samples was dried at 120 °C in Ar atmosphere for 2 h (7 °C min^{-1}), after which the temperature was slowly (5 °C min^{-1}) increased to 700 °C, where the annealing continued for 2 h more in the NH_3 flow (100 mL min^{-1}). Finally, NH_3 flow was switched to Ar flow with the same flow rate and the furnace was allowed to room temperature to obtain NG.

2.3. Preparation of NG-TiO_2

NG-TiO_2 (NGT) composite sample were prepared by a hydrothermal method. Firstly, 16 mg of NG was dispersed into 15 mL water with magnetic stirring for 3 days, resulting in a metastable gray dispersion solution. The dispersion was allowed to settle overnight and then the precipitates at bottom were removed. The solution was sonicated for an additional 30 min followed by the addition of 30 mL ethanol. The resultant dispersion was then placed in an ice bath. Meanwhile, a titanium precursor composed of 3 mL titanium (IV) isopropoxide (Aldrich), 5 mL ethanol and 3 mL acetic acid was also placed in an ice bath. The mixture was then added drop-by-drop into the chilled NG aqueous solution under vigorous stirring. Subsequently, the stock solution was transferred to a 100 mL Teflon-lined stainless steel autoclave and heated to 180 ºC for 12 h. A sponge-like black hydrogel compound was obtained after cooled naturally under ambient conditions and was thoroughly washed several times with water and ethanol. The sample was then freeze-dried and annealed at 400 °C for 2 h under N_2 atmosphere to increase the crystallinity. Pure TiO_2 was synthesized using a similar approach without the addition of NG.

2.4. Preparation of Au-NG-TiO_2

Au nanoparticles were photodeposited onto the prepared NG-TiO_2 samples. In order to deposit the 1 wt% Au on NG-TiO_2 composite, a known amount of the NG-TiO_2 composite material and, accordingly, $HAuCl_4 \cdot 3H_2O$ (Sigma-Aldrich) were added to 100 mL of a water-ethanol mixture. The solution described above was purged with N_2 flow for 1 h to remove any dissolved oxygen and generate an inert atmosphere. The solution was irradiated under 300 W Xe lamp with varying the illumination time 5 min, 1 h, and 2 h, samples of ANGT0, ANGT1 and ANGT2 can be obtained, respectively. The precipitate was washed with water and ethanol and then dried via freeze-drying. The procedure for preparation of Au-TiO_2, referred as AT2, was the same to that described in the preparation of ANGT2 except that NG was entirely absent.

2.5. Material Characterizations

X-ray diffraction (XRD) patterns were recorded by X′Pert MPD diffractometer (PANalytical) with Cu Kα radiation, in the 2θ range from 10° to 90°, and using JCPDS database for reference. The samples for scanning transmission electron microscopy (STEM) analysis were prepared by dispersing the prepared catalysts in isopropyl alcohol followed by drop casting the suspension onto a 200-mesh copper grid coated with carbon film. The analytical STEM study carried out using Carl Zeiss Libra 200 FE microscope operated at an accelerating voltage of 200 kV (Cs = 1.2 mm) equipped with an in-column omega-type electron spectrometer. The HRSTEM and HRTEM images were processed using gatan digital micrograph and JEMS software was used to simulate the diffraction pattern to verify the FFT obtain from the Fig. 1(i). The energy-filtered elemental mappings the "three-window method" was used using gatan US1000 CCD camera. The background contribution to the image intensity was obtained from two energy-filtered images ahead of the ionization edge of the element of interest. The determined background
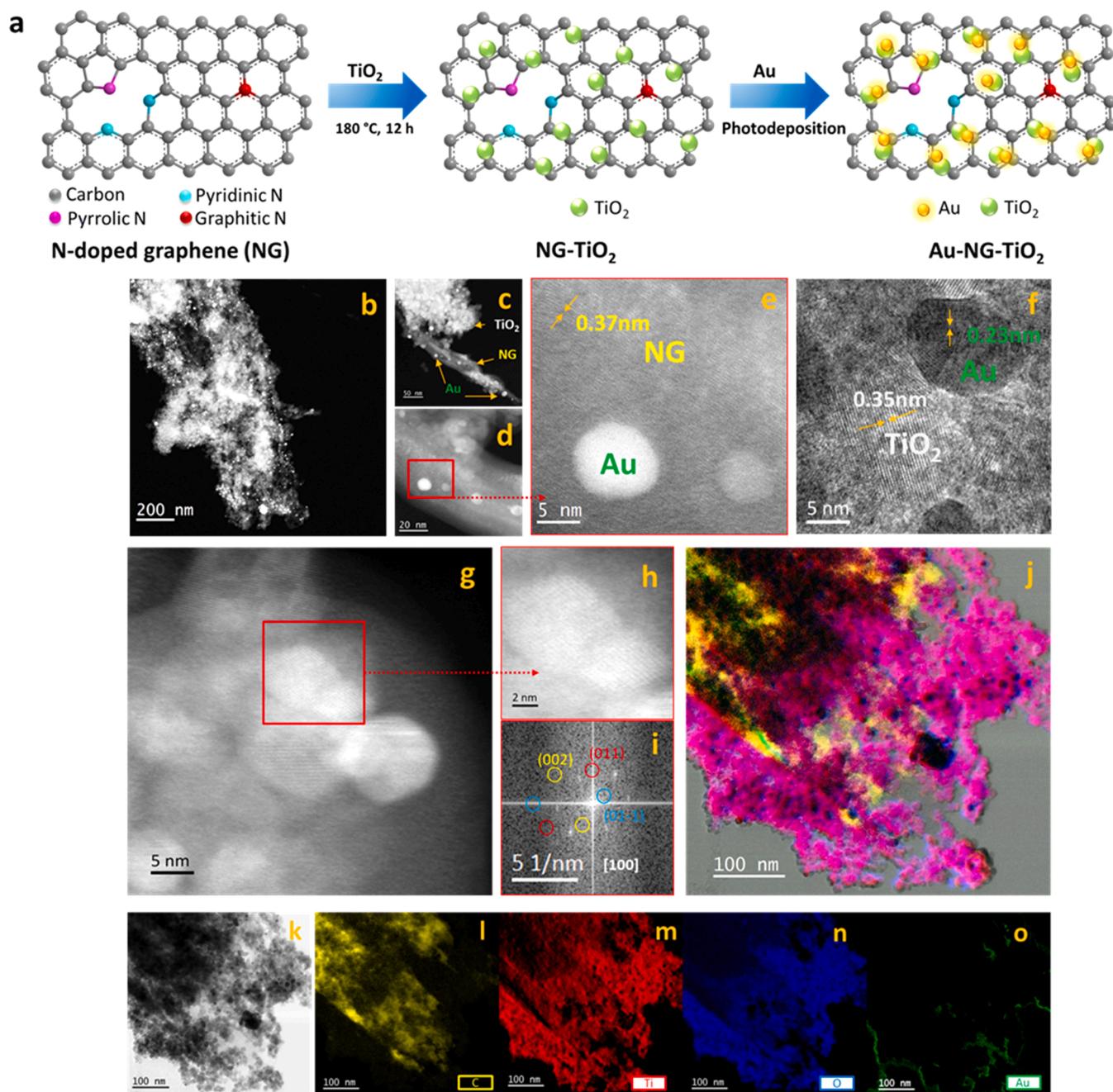
Fig. 1. (a) Schematic illustration of the stepwise synthesis procedure of Au-NG-TiO$_2$. (b-e) The STEM and HRSTEM image of TiO$_2$ and Au NPs dispersed over N-doped graphene. (e) HRSTEM image of N-doped graphene (0.37 nm). (f) HRTEM image of TiO$_2$ and Au NP side by side with the lattice d-spacings of 0.35 nm and 0.23 nm. (g-i) HRSTEM image of TiO$_2$ NP oriented along [100] zone-direction with corresponding FFT image. (i) show the (002) and (011) planes. (j-o) EFTEM elemental maps, (j) Superimposition of EFTEM map, (k) TEM bright field image, (l) EFTEM maps of carbon map (graphene, yellow, K-edge 284), (m, n) Ti (Red, L2, and L3-edge at 462 eV and 456 eV) and O map (Blue, k -edge at 532 eV), (o) Au map (Green). The Au energy loss edges lies close to the plasmon region (O-edge at 54 eV, N-edge at 83 eV) and at weak energy band (M4 and M6 at 2291 eV and 2206 eV).

contribution was subtracted from the third image which was obtained at the ionization edge energy. The Brunauer-Emmett-Teller specific surface area (S$_{BET}$), Pore Volume (V$_{pore}$) and Pore Diameter (D$_{pore}$) were determined from N$_2$ adsorption-desorption isotherms obtained at -196 °C (ASAP 2020, Micromeritics, USA). The optical properties of the samples were analyzed by ultraviolet-visible diffuse reflectance spectra (UV-Vis-DRS) spectrophotometer (Perkin Elmer). The Raman spectra were collected on a Raman microscope (Witec Alpha 300 RA) in the spectral range from 3600 cm^{-1} to 70 cm^{-1}, using a green laser with the excitation wavelength of 532 nm. Single spectra (100X /0,9NA objective) were taken on a number of different positions depending on the

homogeneity of the sample. Laser intensity was kept low enough to avoid laser induced changes or damage to the sample. CO$_2$ sorption capacities were monitored on manometric gas analysis system HTP-IMI Hiden Isochema Inc. Prior to the measurements, the sample was outgassed at 150 °C for 15 h. The CO$_2$ adsorption isotherms were measured up to 1 bar at 25 °C. The X-ray photoelectron spectroscopy (XPS) analyses were carried out on the PHI-TFA XPS spectrometer produced by Physical Electronics Inc equipped with X-ray Al-monochromatic source. The high-energy resolution (HR) spectra were acquired with energy analyzer operating at resolution of about 0.6 eV and pass energy of 29 eV. Low energy electron gun was used to avoid sample charging. XPS

spectra were not shifted for possible charging effect. The accuracy of binding energies was about ± 0.3 eV. Quantification of surface composition was done from XPS peak intensities taking into account relative sensitivity factors provided by instrument manufacturer. Two different XPS measurements were executed on each sample and average composition was calculated. Photoluminescence (PL) spectra of the sample-water suspensions (1 mg mL^{-1}) were recorded using a Synergy H1 microplate reader with monochromator optics (Bio-Tek, USA) at an excitation wavelength of 300 nm in 96 well microplates (Nunc) using top optics. Every sample was measured in several wells and the results were repeatable.

2.6. Photocatalytic CO$_2$ reduction test

The photocatalytic CO$_2$ reduction experiments were carried out in a 100 mL quartz reactor under light irradiation. A commercial solar simulator equipped with a Xenon arc lamp (300 W, Newport) and an AM 1.5 G filter was used as light source. In a typical experiment, 30 mg of the sample was suspended in 10 mL of Milli-Q water and the suspension was sonicated for 30 min to obtain well-dispersed particle suspension. And the suspension was evaporated at 80 °C to form a thin film. Prior to irradiation, the reactor was sealed and purge with nitrogen for 1 h to remove air and ensure that the reaction system was under anaerobic conditions. CO$_2$ was produced by injecting the HCl solution (0.25 mL, 4 M) to react with the NaHCO$_3$ (100 mg) introduced before nitrogen purge. Finally, the sealed quartz reactor was placed under light irradiation. All the photocatalysts were subjected to 4 h light irradiation and gas evolution was measured every hour periodically. The generated gas composition (1 mL) was analyzed with a gas chromatography (GC, SRI-8610 C) equipped with thermal conductivity detector (TCD) and a flame ionization detector (FID) with a methanizer attachment and high purity helium was used as a carrier gas. Standard samples of all potential products were used to identify the calibrations. The standard gas samples (1 mL) exhibited a steady retention time and peak area, from which the unknown products were analyzed by these criterions qualitatively and quantitatively.

2.7. Photoelectro chemical measurements and Computational methodology

This section has been presented in the Supporting Information.

3. Results and discussion

3.1. Characterizations of as-prepared photocatalysts

The multistep preparation process of ternary ANGT photocatalytic system is schematically described in Fig. 1a. As shown in the X-ray diffraction (XRD) patterns (Fig S1a, Supporting Information), all of the samples show identical peaks which can be well matched with anatase TiO$_2$ (JCPDS Card No. 21–1272). Noticeably, no characteristic diffraction peaks for the graphene in the NGT and ANGT composites are observed in the patterns, because of the low amount and weak diffraction intensity of graphene. With both ANGTx and AT2 samples, the weak diffraction peaks at 44.3, 64.5 and 77.5 could be indexed to the (200), (220) and (311) planes of the metallic Au NPs, respectively (JCPDS Card No. 02–1095), indicating that the sizes of the metal NPs are very small. The average crystallite sizes of TiO$_2$ were calculated using Scherrer's equation, from the main diffraction peak of anatase (101). As listed in Table S1, all the samples have almost the same crystallite size (~10–12 nm), suggesting that the introduction of graphene and/or Au into TiO$_2$ has no obvious influence on its crystallite size and morphology, which confirms that the Au NPs are highly dispersed on the surface of the NG-TiO$_2$.[29].

STEM was used to observe the morphology and microstructures of the as-prepared sample. Fig. 1(b-e and g-i) presents the HAADF-STEM images from low magnification to HR-STEM images of the sample ANGT2. It is clearly showing that Au particles are inhomogeneous with a size range between 3 and 35 nm. Au particles sizes between 06 nm and 10 nm are predominantly decorated the TiO$_2$-N-Graphene as evident from the histogram (Fig S7). This substantiates the successful conversion of Au precursor (HAuCl$_4$) to metallic Au NPs, without leaching or agglomeration during the reduction process.[30] A further the observation of HR-STEM image revealed multilayer N-doped graphene with interlayer spacing of 0.37 nm. HR-STEM observation followed FFT analysis of TiO$_2$, one of the TiO$_2$ NP is oriented in [100] zone-axis direction. The lattice planes (002) and (011) can be well witnessed with corresponding d-spacings 0.476 nm and 0.352 nm, respectively. The d-spacings were further confirmed by simulating similar diffraction pattern using JEMS software.[31] The HRTEM image (Fig. 1 f) of the TiO$_2$ and Au NP revealed their lattice spacing of 0.35 nm and 0.23 nm, respectively. Thus, an intimate contact and good incorporation among the Au NPs, TiO$_2$ and N-graphene components, achieved by our multi-step processing condition is believed to favor the transfer of photo-generated electrons between the Au NPs and TiO$_2$ decorated N-graphene, thus enhancing the charge separation and photocatalytic efficiency.[32].

Additional proof from Raman analysis, re-confirmed the co-existence of Au and NG in the ANGT2 composite. The Raman spectra of the TiO$_2$, AT2, and ANGT2 samples were characterized by the presence of bands at E$_g$, B$_{1 g}$, A$_{1 g}$, and E$_g$, indicating the existence of anatase TiO$_2$ in these samples, which is in good agreement with the XRD results.[33] Furthermore, as for ANGT2, another two peaks positioned at 1358 and 1600 cm^{-1}, which represent the D and G bands of graphitized structures are also observed, respectively. The two peaks for D and G band of the ANGT2 are slightly blue-shifted compared with the D band (1355 cm^{-1}) and the G band (1587 cm^{-1}) of NG (Fig. 2a), which is similar to the previous reports.[34] Such a blue shift is possibly due to the charge transfer between TiO$_2$ and graphene nanosheets which indirectly provides evidence for the intimate contact between two of them.[35] However, the characteristic E$_g$ (147 cm^{-1}) peak shifts to larger Raman shift of E$_g$ (156 cm^{-1}) in the ANGT2 (inset of Fig. 2b), ascribed to the surface enhanced Raman scattering effect due to the successful encapsulation of Au NPs into NG-TiO$_2$ composites, which is consistent with the TEM results.[36] The fairly high intensity of the D-band indicates the presence of structural defects in the graphene layer by nitrogen doping. The I$_D$/I$_G$ ratio calculated for bare NG was 1.27, while that for ANGT2 was 1.06. As shown in Fig. 2c, optical light absorption properties in the visible region are significantly enhanced with ANGT2 once NG is introduced.[37] Nitrogen adsorption–desorption isotherms and the corresponding pore size distributions of ANGT2 and AT2 samples are shown in Fig. 2d. The samples exhibited a type-IV adsorption-desorption isotherm, characteristic of mesoporous materials, with a H2 type hysteresis loop. It is interesting to note that ANGT2 composite with the optimum graphene content and integrated Au NPs show the highest surface area of 166 m^2 g^{-1} over that of AT2, which in turn shows the activity for the PCO$_2$R. In addition, the detailed Brunauer-Emmett-Teller (BET) Surface area (S$_{BET}$), pore parameters are displayed in Table S1.

Besides, X-ray photoelectron spectroscopy (XPS) measurement was carried out to substantiate the existence of characteristic elements and chemical states on the surface of NG, AT2 and ANGT2 samples (Figs. 3a–f and S2–3). The survey spectrum of ANGT2 (Fig. 3a) clearly indicated the coexistence of C 1 s, N 1 s, Ti 2p, O 1 s, and Au 4 f elements in the sample, and the elemental contents are listed in Table S2. For the C 1 s spectrum (Fig. 3b), the small peak located at 284.1 eV is assigned to C=C, which may originate from the strong interaction between NG and TiO$_2$. Another three peaks are located at 285.2, 286.6, and 289.1 eV, correspond to the C−C, C−N, and C=O groups, respectively. The N 1 s peak at 400.3 eV (Fig. 3c), could be deconvoluted to three peaks with binding energies at 398.1, 400.2 and 401.7 eV, which were attributed to pyridinic N, pyrrolic N and graphitic N, respectively.[38] The weak signal intensity of N 1 s on the ANGT2 sample was observed as compared
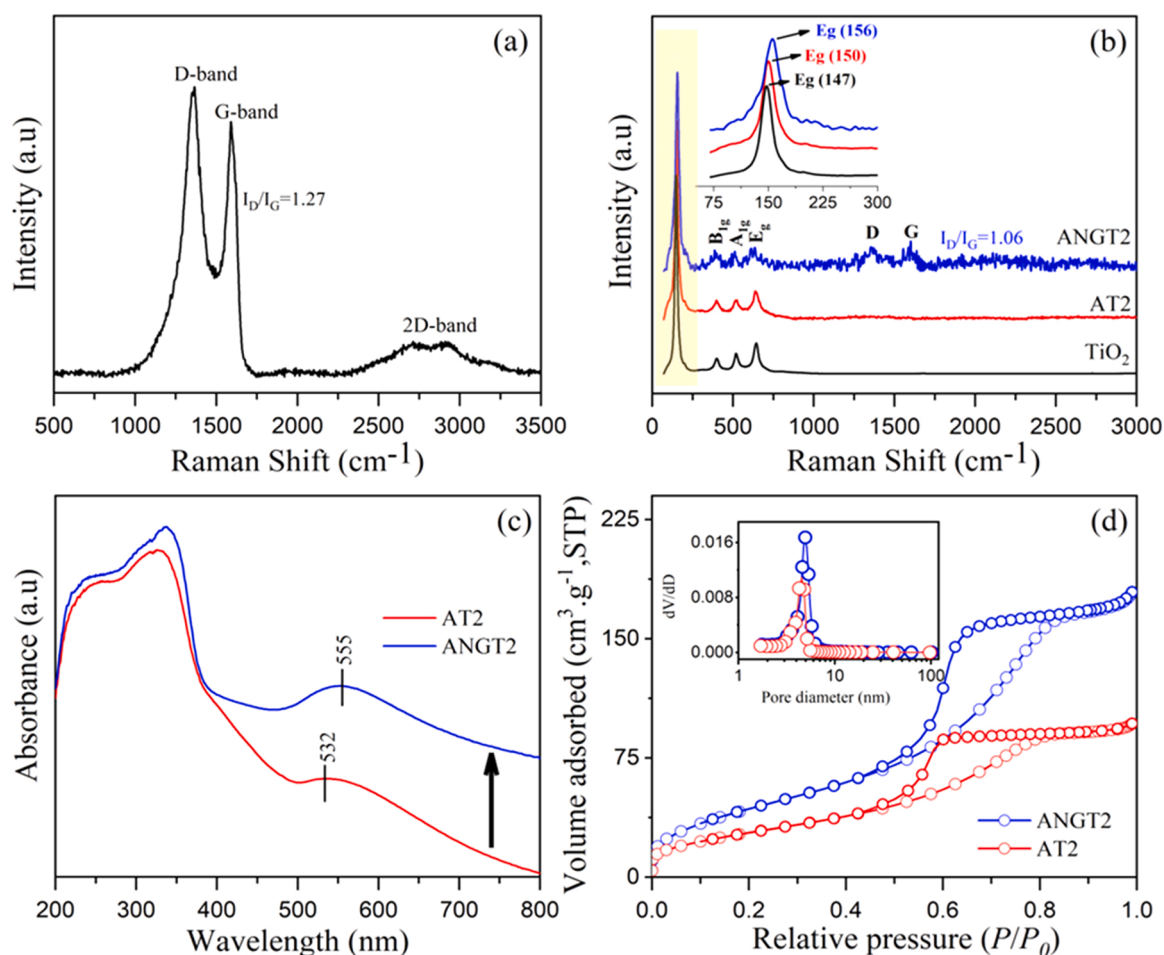
Fig. 2. (a) Raman spectra of N-doped graphene, (b) Raman spectra of TiO_2, AT2 and ANGT2, (c) UV-Vis-DRS spectra of AT2 and ANGT2, (d) N_2 adsorption-desorption isotherms (inset: pore size distribution) of AT2 and ANGT2.
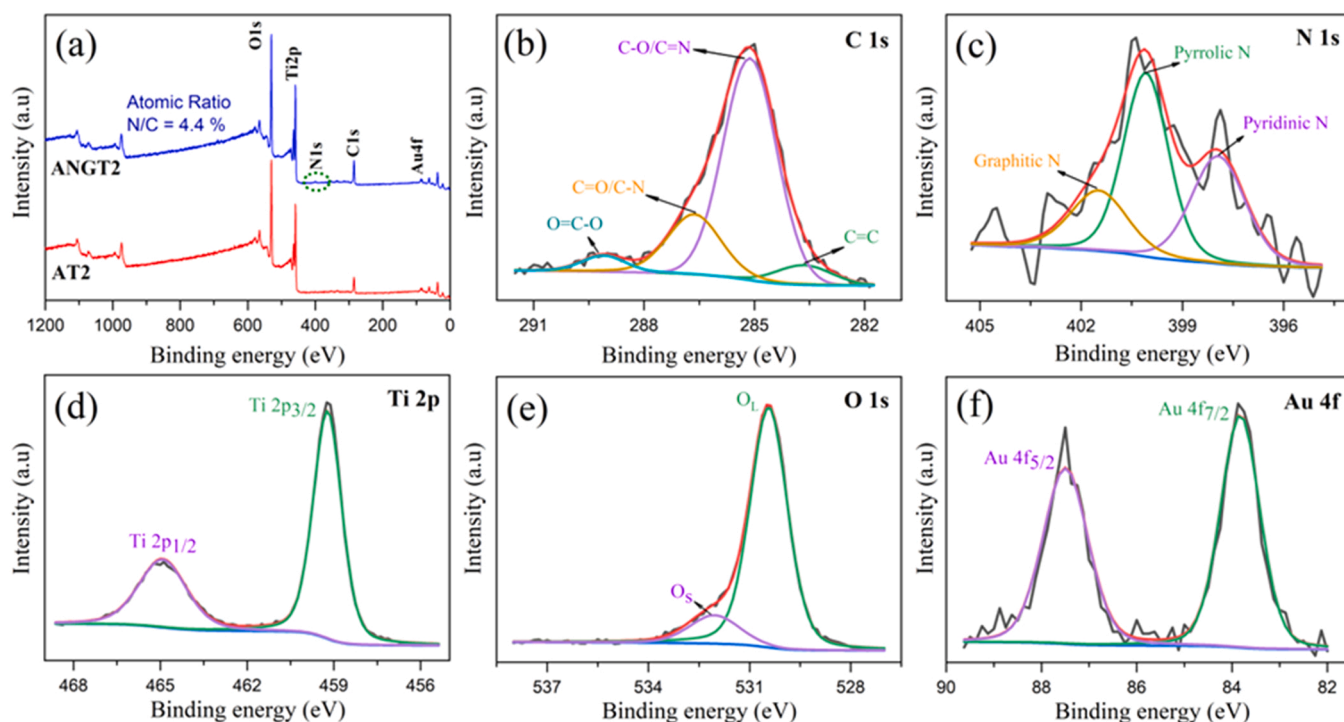

Fig. 3. (a) The full-scan XPS spectrum of ANGT2 and AT2, (b-f) High resolution XPS spectra of the C 1 s, N 1 s, Ti 2p, O 1 s, and Au 4 f recorded for the ANGT2.

to bare NG, certainly due to the low content of NG. The atomic ratio of N/C is 7.5% (Fig S2), which is larger than that of N-doped graphene prepared by other methods (0.3–5.6%), thus indicating the effectiveness of N doping by our method.[38,39] For the HR-XPS spectra of Ti 2p region (Fig. 3d), the two prominent peaks centered at 459.1 and 464.9 eV correspond to Ti $2p_{3/2}$ and Ti $2p_{1/2}$ energies of Ti^{4+} in TiO_2, respectively. The ANGT2 sample did not show any significant peak shift in these characteristic binding energies, indicating that there is no chemical environment modification for Ti^{4+}.[41] Two kinds of O species were observed for ANGT2 after deconvolution of the O 1 s spectrum (Fig. 3e), with binding energies (BEs) located at 530.4 and 532 eV, which are assigned to the lattice oxygen (O_L) and surface-adsorbed oxygenated species (O_S), such as -OH and H_2O, respectively[40] As shown in Fig. 3f, the Au 4 $f_{7/2}$ core level is located at 83.8 eV, which is slightly lower in BE as compared to the standard value reported for metallic state of Au at 84 eV. A decrease in BE (0.2 eV) indicating the charge transfer from the TiO_2 lattice to the Au.[41] This trend correlates well with the Raman results, which show a significant blue shift for the Eg mode upon Au deposition.

In order to explore the separation efficacy and transfer behavior of photoinduced charges in photocatalyst, photoluminescence (PL), transient photocurrent response (TPR), and electrochemical impedance spectra (EIS) were executed. The emission band located at 405 nm is assigned to the free exciton emission of TiO_2 (Fig. 4a). Quenching of the PL intensity in ANGT2 suggests the improved mobility of the carriers, due to the introduction of NG in ANGT2 sample, which may favor the separation of photogenerated e-h pairs, thus decreasing the charge carrier recombination rate, and the efficient suppression of recombination rate of the photogenerated e-h was crucial for enhancing the photocatalytic activities.[42] As shown in Fig. 4b, both AT2 and ANGT2 displayed enhanced transient photocurrent responses within the light on–off cycles, which provided clear evidence on the efficient separation and transfer of charge carriers.[43,44] It is clear that the photocurrent intensity of ANGT2 was twice that of AT2 under visible light illumination, indicating more effective charge separation in ANGT2 as compare to AT2. In addition, the charge transfer of ANGT2 and AT2 in the dark was studied by electrochemical impedance spectra (Fig. 4c). The Nyquist plots clearly indicate that the charge transfer resistance decreased for the ANGT2 due to the excellent conductivity of NG. The pronounced decrease in the charge-transfer resistance implies the accelerated electron transfer in this sample, which should enhance the photocatalytic efficiency.[45].

3.2. PCO_2R activity measurements

The adsorption of CO_2 on the surface of the photocatalyst is the main critical process for the PCO_2R. As shown in Fig. 5a, while the AT2 sample showed CO_2 uptake capacity only 9.52 mg g^{-1}, the ANGT2 sample on the other hand exhibited high value of 12.74 mg g^{-1}. This suggests the strong interactions between ANGT2 and CO_2 molecules due to the high CO_2 adsorption activity of NG. The high affinity of ANGT2 toward CO_2 means that more CO_2 would be trapped and/or activated by the active sites on the surface, which may facilitate further reduction of CO_2 when NG is used as a catalyst or catalyst support. Moreover, graphene is an excellent CO_2 adsorbent with a theoretical maximum uptake of 37.93 wt %.[46] The photocatalytic activity of the developed ternary ANGTx heterostructure catalysts for the PCO_2R to solar fuels was determined in the gas phase under batch conditions. Control experiments conducted without photocatalyst and/or light illumination found no products formed, thus demonstrating the critical roles of photocatalyst and light illumination for the PCO_2R. As can be seen in Fig. 5b, the photocatalytic activity of ANGTx heterostructure catalysts studied is strongly affected by the photodeposition time and the detailed catalytic performance data are summarized in Table S3. It indicated that ANGTx heterostructure catalysts exhibited significant PCO_2R, affording CH_4 as the sole carbonaceous product together with low yield of CO, C_2H_2 and C_2H_6 evolution evidenced by GC spectra (Fig S4). It is worth noting that NG in ANGTx photocatalysts is also beneficial for C_2 hydrocarbon production. The amount of product generation increased linearly with time during the photocatalytic reactions are provided in Fig S5. Quantitatively, the production rate of CH_4, CO, C_2H_2 and C_2H_6 over ANGT2 are the highest among all the samples, reaching 83.72, 2.18, 6.15 and 0.47 µmol g^{-1} h^{-1}, respectively. In comparison, the binary AT2 photocatalyst provided an inefficient activity towards CH_4 (1.22 µmol g^{-1} h^{-1}) and CO (1.03 µmol g^{-1} h^{-1}) production. From the aspect of electron consumption rate ($R_{electron}$) for the reduced products, calculated by taking the number of consumed electrons per product molecule into account, the value was 742.39 µmol g^{-1} h^{-1} for ANGT2, which is more than 4 times that of ANGT0, or 60 times that of AT2. Notably, to the best of our knowledge, this is the highest rate of PCO_2R ever reported in the literature. Therefore, it can be deduced that N-graphene promotes the predominant generation of CH_4 in this ANGT2 photocatalytic system, which could be ascribed to the outstanding ability of N-graphene as a very good electron transfer mediator and adsorber for CO_2. Furthermore, the catalytic stability of ANGT2 was also tested by recycling it in a refreshed reaction condition every 4 h of continuous PCO_2R (Fig. 5c). After cycling 3 times, no obvious decay was obtained. The powder X-ray diffraction profile further confirmed that the structure of ANGT2 was retained after
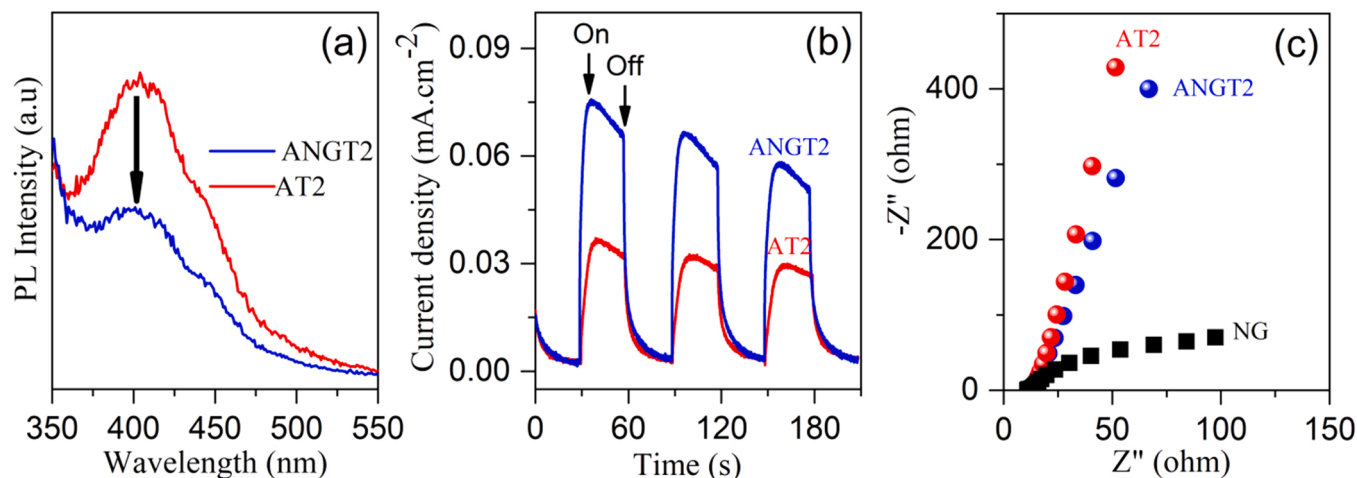

Fig. 4. (a) Steady state PL specta with an excitaion wavelength of 300 nm (b) Transient photocurrent responses measured under visible light illumination and (c) EIS spectra of NG, ANGT2 and AT2.
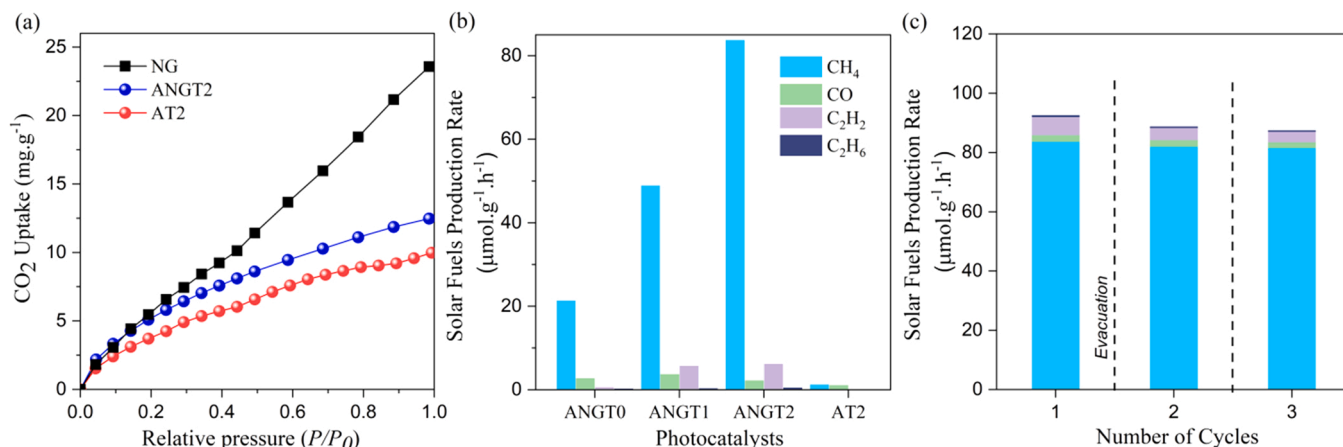
Fig. 5. (a) CO_2 adsorption capacity isotherms at 25 °C, (b) Solar fuel production rate for ANGT0, ANGT1, ANGT2 and AT2 (production rate was derived following 4 h of light irradiation), (c) recycling test of ANGT2 during 3 cycles.

reused for 3 cycles (Fig S1b). Also, the PCO_2R activity of our ANGT2 catalyst shows superior performance can be compared with to other previously reported typical photocatalysts in gas phase (see Table S4, Supporting Information). These results demonstrate the very high activity, stability and recyclable capacity of the ANGT2 in catalyzing CO_2 reduction into value added solar fuels especially methane under visible-light irradiation.

3.3. Mechanism analysis

To understand the difference in catalytic activity between the AT2 and ANGT2, UV-Vis-DRS, Mott-Schottky plots and XPS valance band spectra were conducted to elucidate their bandgaps, positions of flat band potential and valance band maxima (VBM), respectively. The corresponding bandgaps were calculated using the well-known Tauc method obtained from UV-Vis-DRS, as shown in Fig. 6a. It can be seen that ANGT2 and AT2 presents a narrower band gap than NGT, which results from the incorporation of Au NPs into the framework of TiO_2 and TiO_2-N-graphene causing a red-shift of the intrinsic absorption edge in UV-Vis-DRS due to the surface plasmon resonance (SPR).[47] As illustrated in Fig. 6b, the positive slopes of the obtained C^{-2} values (vs the applied potentials) at frequency of 1.7 kHz depict the typical characteristic of n-type semiconductors. The flat band position is consistent with the intersection point of the frequency, which were approximately − 0.58, − 0.62 and 0.50 V versus the saturated Ag/AgCl reference electrode (pH=7) for AT2, ANGT2 and NGT, respectively (−0.38, −0.42 and −0.30 V vs. NHE). It is generally accepted that the conduction band

minima (CBM) are very close to the flat band potential in n-type semiconductors.[48–50] Based on the flat band edge potentials, the CBM of AT2, ANGT2 and NGT were determined to be at − 0.58, − 0.62 and − 0.50 V vs. NHE, respectively. In XPS, not only the information on the BE of a specific element can be obtained but also the total density of states (DOS) of the VBM. Fig. 6c shows the valence band XPS spectra of the AT2, ANGT2 and NGT photocalysts, which were determined to be 1.60, 2.30 and 2.70 eV, respectively. A decrease of binding energies for the samples AT2 and ANGT2 in comparison with NGT, indicates the charge transfer from the TiO_2 lattice to the Au clusters. This observation well correlates with Raman spectra, which show a significant red shift for the E_g feature upon Au deposition.

It is well known that PCO_2R mainly involves the generation of charge carriers, charge carrier transfer and multielectron chemical reduction at a particular potential. In our system, all these three important aspects were considered during the design of the photocatalysts. Based on the results, a plausible mechanism of visible-light-driven PCO_2R over ANGT photocatalyst is proposed as follows. According to the band structure alignments exemplified in Fig. 7a, the CBM of ANGT2 shifts to more negative value than that of AT2 and NGT which can be attributed to the quantum confinement effects induced by nanostructure. These CBM positions meet the thermodynamic requirement for the PCO_2R to hydrocarbons. Specifically, multielectron reduction processes are involved in the production of CH_4, CO, C_2H_2 and C_2H_6, in our experiment. Overall, the band edge plot indicates that the deposition of Au on TiO_2-NG heterostructure system pushes both the conduction and valence band edge of ANGT2 towards more negative potential.[51] The assumed
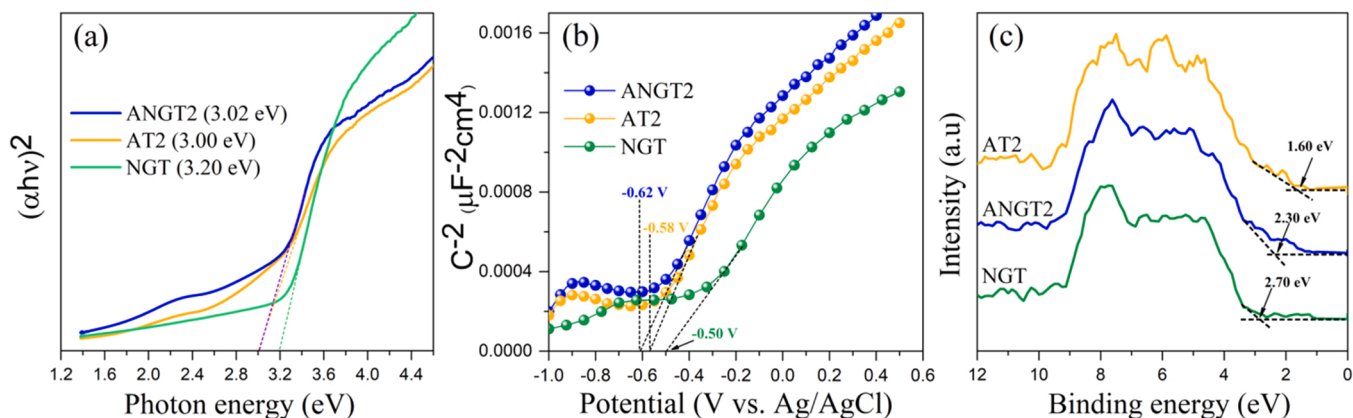

Fig. 6. (a) Tauc's plot of ANGT2, AT2 and NGT heterostructure samples. (b) Mott-Schottky plots collected at 1.7 kHz of ANGT2, AT2 and NGT versus the saturated Ag/AgCl reference electrode (pH = 7) (c) Valance band spectra of ANGT2, AT2 and NGT.
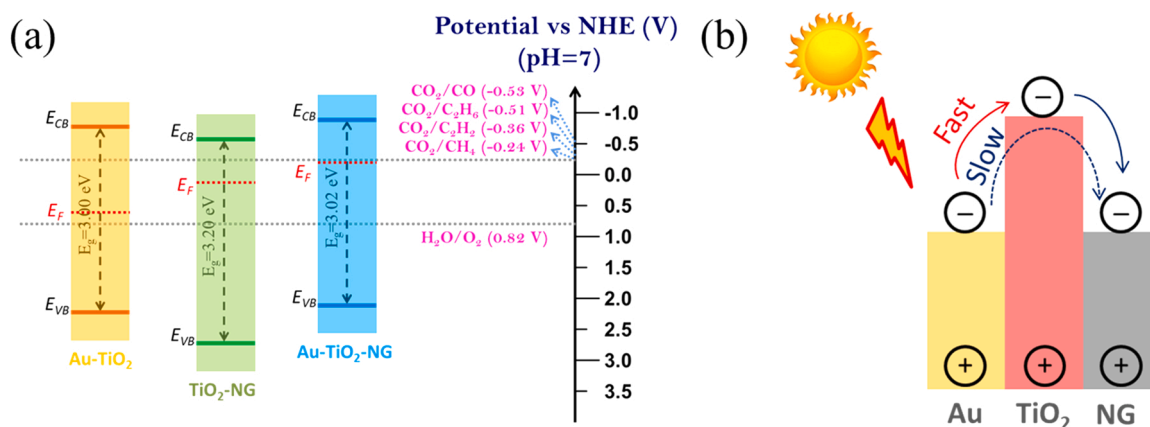
Fig. 7. (a) Schematic band structure of Au-TiO$_2$, TiO$_2$-N-doped graphene and Au-TiO$_2$-N-doped graphene, respectively. (b) Schematic representation of the proposed mechanism illustrating the charge separation and transportation in the Au-TiO$_2$-N-doped graphene photocatalyst under light illumination.

synergism between the Au NPs, N-doped graphene, and TiO$_2$ and the possible charge transfer mechanism in the ANGT2 system have been elucidated in Fig. 7b. Upon visible-light irradiation, Au NPs are photo-excited under light irradiation, due to plasmonic resonance, and charge separation is accomplished by the transfer of photo-excited electrons from the Au NPs to the conduction band of TiO$_2$. The hot electrons in TiO$_2$ are then transferred to the N-graphene sheets, in agreement with the lower redox potential of graphene as compared to

TiO$_2$.[45] A superior charge transfer efficiency was accordingly evidenced in the presence of Au and NG in TiO$_2$ system (Fig. 4b). Due to the high electron-accepting nature of N-graphene, may also directly accept hot electrons from Au in the excited state. However, the hot electron transfer and corresponding transfer efficiency from Au to NG is relatively low compared with the transfer efficiency from Au to TiO$_2$. This process remains key factor to reduce the recombination of energetic species that are not rapidly transferred from Au to TiO$_2$. The charge
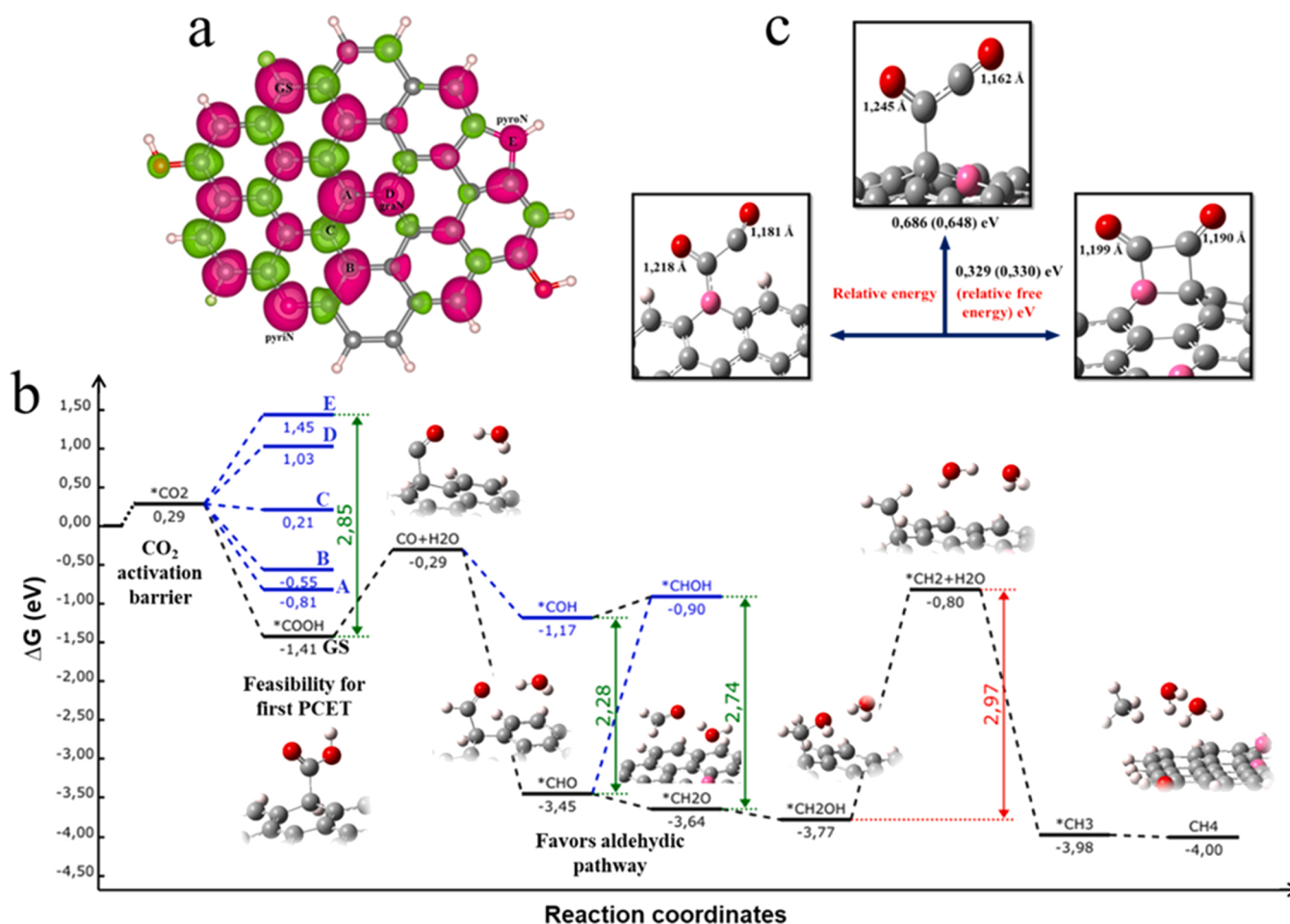

Fig. 8. (a) Spin density distribution in NGO (with oxygen functionalities). Pink lobes represent positive spin density and the green represents the negative spin density lobes, plotted with the isosurface value of 0.001 using VESTA. (b) Calculated free-energy diagram for CO$_2$ reduction to CO and CH$_4$ on the ANGT catalyst, as well as the adsorption configurations of key intermediates. (c) Feasible pathways for the CO-dimerization.

separation is therefore assumed to occur at both Au-NG and Au-TiO$_2$ interfaces. Thus, both the interfaces can function as active sites, where the adsorbed CO$_2$ captures electron to form CO$_2$ radical anions. Then, adsorbed CO$_{ads}$ may form after series of proton-coupled multielectron reactions with CO$_2$ radical anions. The strong interaction between CO$_{ads}$ and the ANGT2 photocatalyst can prevent CO to escape from the photocatalyst surface, confirmed by the fact that low yield of CO was detected in the products, which is favorable to the further hydrogenation of CO$_{ads}$ to generate more CH$_4$. Therefore, charge separation at the ANGT2 interface and suppression of carrier recombination can be realized, which leads to an enhanced PCO$_2$R on the ANGT2. Consequently, the emerging understanding of mechanism for such ANGT2 photocatalyst should bring promise to the fulfillment of actual applications in the near future.

3.4. Theoretical calculation of PCO$_2$R reaction path

To explain and understand the product distribution of the ANGT catalysts in PCO$_2$R, density functional theory (DFT) calculations were performed to illustrate the reaction network from CO$_2$ photoreduction into C$_1$ and C$_2$ hydrocarbons. In hetero-atom doped graphene systems, it is well-known that the catalytic activity stems from the asymmetric (positive) spin and charge density distribution due to hetero-atoms in the lattice.[52–54] On the basis of this, we discern the catalytically active centers with the aid of spin density distribution. We have studied the spin density mapping on finite pristine-NG (model in Fig S6) as well as on NG with oxygen (NGO) functionalities (Fig. 8a). Analysis of the spin density distribution of pristine-NG and the NGO functionalities is in accordance with the reported literature and did not affect the spin density distribution at the basal-plane as well as at the edge-plane. To highlight the role of positive spin-density as well the role of the other carbon and nitrogen centers being the active sites for the PCO$_2$R, we have considered the following sites; viz, pyridinic-nitrogen site as pyriN, graphitic-nitrogen site as graN (labeled as D), pyrrolic-nitrogen site as pyroN (labeled as E), basal-plane carbon atom with negative spin density labeled as site C, basal-plane carbon atom with positive spin density labeled as site B, basal-plane carbon atom adjacent to graN with positive spin density labeled as site A, and the edge-plane carbon atom with positive spin density labeled as GS. All the labels mentioned are as depicted in Fig. 8a. For the photocatalytic CO$_2$ reduction, the catalytic active centers are discerned with the aid of spin density mapping of the NGO (as shown in Fig. 8a), and are further validated by the adsorption free energy change of the reactive intermediate (RI), *COOH. This is the first and most important RI in catalytic reduction of CO$_2$ formed by first proton-coupled electron transfer. Feasibility of further reduction into solar fuels depends primarily on the stabilization of this *COOH. Herein, we differentiate this process by correlating the adsorption free energy with spin density distribution and are plotted in Fig. 8b for the whole reaction coordinate till the formation of methane.

Meticulously, Zou *et al* have illustrated that how nitrogen-doped graphene quantum dots (NGQDs) electrocatalyzes CO$_2$ to hydrocarbons and liquid oxygenates, bringing out the correlation from the product distribution on copper surface.[55] Pyridinic sites (pyriN) in NGQDs were shown to catalyze the electroreduction of CO$_2$ to C$_1$ and C$_2$ products, by stabilizing the *COOH and with further second PCET to yield CO and/or formic acid. To determine the most suitable site (with lowest free energy change) for the stabilization of this RI on NGO, we considered seven different sites as described earlier and depicted in Fig. 8b. The free energy change (ΔG) on pyriN and GS site is found to be − 1.37 eV and − 1.41 eV respectively. As the energies are very close, it is clear that edge carbon atom with positive spin density is also stabilizing *COOH on par with pyriN. Further, it is already known that the pyriN sites are catalytically active, so we then explored the catalytic activity of edge carbon atom as well as the other carbon atoms with positive spin density. Charge and spin density analysis on the selected sites are tabulated in Table S5.

It is obvious from the Table S5 and the Fig. 8b that, the *COOH is stabilized with sites not only by pyriN but also via carbon atoms with positive spin density. The lowest free energy change is shown by site GS and further, second PCET to *COOH leads to the formation of CO (as confirmed by the experiments). Hence, we only considered the edge carbon atom (labeled as GS) to study further six PCET to CO on NGO for the further formation of methane. Nevertheless, CO is the most important RI for the feasible formation of solar fuels on any (photo/electro) catalyst surfaces viz, metal/metal oxide/non-metal or even at the metal-free interfaces.[56] PCET to CO is again the crucial step which bifurcate the pathways for hydrocarbons and liquid oxygenates. On NGO, we also found that it proceeds via lowest energy *CHO pathway rather than *COH pathway. The free energy changes depicted in Fig. 8b, clearly show that *COH pathway is not feasible comparatively. Fourth PCET leads to the formation of formaldehyde rather than *CHOH and the corresponding barrier of 2.74 eV is shown in Fig. 8b. Thermodynamically demanding step is the sixth PCET for the formation of *CH$_2$ with H$_2$O (*CH$_2$-H$_2$O). The complexity of this particular step has also been highlighted by Zou et.al, in the case of NGQDs bringing the differences on metal and metal-free interfaces. Further, barriers for each step could have also been reduced by invoking few terms in the free energy equation like the CHE model to include pH and potential corrections. [57] Nevertheless, all the calculations presented in this work are with the ground state DFT, without including and invoking any excited state calculations and in principle, detailed description of photocatalytic reaction mechanism is computationally challenging by employing time-dependent DFT based methodologies. Finally, two subsequent PCET to *CH$_2$ leads to the formation of methane on NGO, as depicted in Fig. 8b.

In addition, on this particular interface of NGO, acetylene has also been detected and quantified experimentally. This comes from the feasibility of CO dimerization on this interface. Limiting ourselves, a) with the calculation of many PCET steps for the complete understanding of free energy landscapes for the formation of acetylene, and b) the complexity associated with various bifurcation pathways from the dimerized-CO on NGO for acetylene production, so we only perform the calculations on the feasibility of CO-dimerization over NGO via pyridinic nitrogen and/or neighboring carbon atoms. For the calculation of relative energy and relative free energy, CO-dimerization via pyridinic nitrogen is considered as reference state.55 This CO-dimerization over NGO, as described in Fig. 8c, is the most important step and crucial for the selective production of solar fuels/hydrocarbons.

4. Conclusions

In summary, we demonstrate a series of Au-TiO$_2$ decorated N-doped graphene (ANGT-*x*) heterostructure photocatalysts successfully synthesized by multistep preparation process, which exhibited significant enhancement for visible light driven CO$_2$ reduction toward solar fuel with high selectivity for methane production using a gas-phase, batch reactor system. The successful fabrication of the ternary composite catalyst was confirmed by XRD, STEM, Raman, and XPS analysis. Improved optical properties and smooth charge migration among the catalysts were indicated by UV-Vis-DRS, PL, TPR and EIS analysis. Experimental results corroborated with theoretical DFT studies validated the unique ability of N-graphene playing a key role in efficiently reducing the Gibbs free energy of PCO$_2$R reaction kinetics, increasing the binding strength of *COOH intermediate and improved charge transfer process. In contrast to the conventionally reported binary catalysts, the synergistic coordination facilitated by the unique coupling of high photoactivity TiO$_2$ with LSPR effect of Au NPs and excellent electronic transport plus CO$_2$ adsorption properties of N-doped graphene resulted in high efficiency photocatalytic CO$_2$ reduction by the optimized sample ANGT2 delivering highest R$_{electron}$ value of 742.39 μmol g^{-1} h^{-1} in 4 h under the visible-light irradiation. More importantly, the achieved catalytic activity was ~4 and ~60 folds

higher than that of ANGT0 and binary AT2 catalysts, respectively. The exceptional catalytic performance of ANGT2 is accredited to the well-defined assembly and seamless interfacial contact among the plasmonic Au NPs, TiO_2 and N-doped graphene components that favored concomitant enhancement of light absorption, CO_2 adsorption together with improved charge transfer kinetics and efficient suppression of photogenerated (e-h) recombination. The illustrated mechanism and the enhanced photocatalytic efficiency of ternary ANGT*x* catalysts pave way for the development of future ternary hybrid solar fuel photocatalysts based on NG.

CRediT authorship contribution statement

Khaja Mohaideen Kamal: Investigation, Conceptualization, Data curation, Methodology, Project administration, Resources, Formal analysis, Writing-original draft, Writing-review & editing. **Rekha Narayan:** Conceptualization, Methodology, Resources. **Narendraraj Chandran:** Data curation, Formal analysis, Resources. **Stefan Popović:** Data curation, Formal analysis, Resources. **Mohammed Azeezulla Nazrulla:** Data curation, Formal analysis, Resources. **Janez Kovač:** Formal analysis, Resources. **Nika Vrtovec:** Resources. **Marjan Bele:** Resources. **Nejc Hodnik:** Formal analysis, Resources. **Marjeta Maček Kržmanc:** Resources. **Blaž Likozar:** Conceptualization, Writing-review & editing, Supervision, Project administration, Resources, Funding acquisition.

Declaration of Competing Interest

The authors declare that they have no known competing financial interests or personal relationships that could have appeared to influence the work reported in this paper.

Acknowledgement

Appendix A. Supporting information

Supplementary data associated with this article can be found in the online version at doi:10.1016/j.apcatb.2022.121181.

References

[1] X. Chang, T. Wang, J. Gong, CO_2 photo-reduction: Insights into CO_2 activation and reaction on surfaces of photocatalysts, Energy Environ. Sci. 9 (2016) 2177–2196.

[2] H. Pang, X. Meng, P. Li, K. Chang, W. Zhou, X. Wang, X. Zhang, W. Jevasuwan, N. Fukata, D. Wang, J. Ye, Cation vacancy-initiated CO_2 photoreduction over ZnS for efficient formate production, ACS Energy Lett. 4 (2019) 1387–1393.

[3] X. Zhang, D. Kim, J. Yan, L.Y.S. Lee, Photocatalytic CO_2 reduction enabled by interfacial S-scheme heterojunction between ultrasmall copper phosphosulfide and g-C_3N_4, ACS Appl. Mater. Interfaces 13 (2021) 9762–9770.

[4] M. Liu, Y.-F. Mu, S. Yao, S. Guo, X.-W. Guo, Z.-M. Zhang, T.-B. Lu, Photosensitizing single-site metal-organic framework enabling visible-light-driven CO_2 reduction for syngas production, Appl. Catal. B 245 (2019) 496–501.

[5] X. Li, X. Wu, S. Liu, Y. Li, J. Fan, K. Lv, Effects of fluorine on photocatalysis, Chin. J. Catal. 41 (2020) 1451–1467.

[6] K. Li, S. Zhang, Y. Li, J. Fan, K. Lv, MXenes as noble-metal-alternative co-catalysts in photocatalysis, Chin. J. Catal. 42 (2021) 3–14.

[7] J. Ran, M. Jaroniec, S.-Z. Qiao, Cocatalysts in semiconductor-based photocatalytic CO_2 reduction: Achievements, challenges, and opportunities, Adv. Mater. 30 (2018), 1704649.

[8] S. Wang, B.Y. Guan, X.W. Lou, Rationally designed hierarchical N-doped carbon@ $NiCo_2O_4$ double-shelled nanoboxes for enhanced visible light CO_2 reduction, Energy Environ. Sci. 11 (2018) 306–310.

[9] S. Guo, H. Zhang, Y. Chen, Z. Liu, B. Yu, Y. Zhao, Z. Yang, B. Han, Z. Liu, Visible-light-driven photoreduction of CO_2 to CH_4 over N,O,P-containing covalent organic polymer submicrospheres, ACS Catal. 8 (2018) 4576–4581.

[10] W.-J. Ong, L.K. Putri, A.R. Mohamed, Rational design of carbon-based 2D nanostructures for enhanced photocatalytic CO_2 reduction: A dimensionality perspective, Chem. Eur. J. 26 (2020) 9710–9748.

[11] M.-Q. Yang, Y.-J. Xu, Photocatalytic conversion of CO_2 over graphene-based composites: Current status and future perspective, Nanoscale Horiz. 1 (2016) 185–200.

[12] Y. Chen, G. Jia, Y. Hu, G. Fan, Y.H. Tsang, Z. Li, Z. Zou, Two-dimensional nanomaterials for photocatalytic CO_2 reduction to solar fuels, Sustain. Energy Fuels 1 (2017) 1875–1898.

[13] Y. Hou, Z. Wen, S. Cui, S. Ci, S. Mao, J. Chen, An advanced nitrogen-doped graphene/cobalt-embedded porous carbon polyhedron hybrid for efficient catalysis of oxygen reduction and water splitting, Adv. Funct. Mater. 25 (2015) 872–882.

[14] L.-Y. Lin, Y. Nie, S. Kavadiya, T. Soundappan, P. Biswas, N-doped reduced graphene oxide promoted nano TiO_2 as a bifunctional adsorbent/photocatalyst for CO_2 photoreduction: Effect of N species, Chem. Eng. J. 316 (2017) 449–460.

[15] Y. Li, M. Gu, X. Zhang, J. Fan, K. Lv, S.A.C. Carabineiro, F. Dong, 2D g-C_3N_4 for advancement of photogenerated carrier dynamics: Status and challenges, Mater. Today 41 (2020) 270–303.

[16] L. Qu, Y. Liu, J.B. Baek, L. Dai, Nitrogen-doped graphene as efficient metal-free electrocatalyst for oxygen reduction in fuel cells, ACS Nano 4 (2010) 1321–1326.

[17] J. Liang, L. Li, Synthesis of N-doped graphene-functionalized Zn1.231Ge0.689N1.218O0.782 solid solution as a photocatalyst for CO_2 reduction and oxidation of benzyl alcohol under visible-light irradiation, J. Mater. Chem. A 5 (2017) 10998–11008.

[18] C. Bie, B. Zhu, F. Xu, L. Zhang, J. Yu, In situ grown monolayer N-doped graphene on CdS hollow spheres with seamless contact for photocatalytic CO_2 reduction, Adv. Mater. 31 (2019), 1902868.

[19] Z. Mou, Y. Wu, J. Sun, P. Yang, Y. Du, C. Lu, TiO_2 nanoparticles-functionalized N-doped graphene with superior interfacial contact and enhanced charge separation for photocatalytic hydrogen generation, ACS Appl. Mater. Interfaces 6 (2014) 13798–13806.

[20] L.-L. Tan, W.-J. Ong, S.-P. Chai, A.R. Mohamed, Noble metal modified reduced graphene oxide/TiO_2 ternary nanostructures for efficient visible-light-driven photoreduction of carbon dioxide into methane, Appl. Catal. B 166 167 (2015) 251–259.

[21] E. Cortés, L.V. Besteiro, A. Alabastri, A. Baldi, G. Tagliabue, A. Demetriadou, P. Narang, Challenges in Plasmonic Catalysis, ACS Nano 14 (2020) 16202–16219.

[22] S. Linic, S. Chavez, R. Elias, Flow and extraction of energy and charge carriers in hybrid plasmonic nanostructures, Nat. Mater. 20 (2021) 916–924.

[23] K. Li, S. Zhang, Q. Tan, X. Wu, Y. Li, Q. Li, J. Fan, K. Lv, Insulator in photocatalysis: Essential roles and activation strategies, Chem. Eng. J. 426 (2021), 130772.

[24] G. Halasi, G. Schubert, F. Solymosi, Photodecomposition of Formic acid on N-doped and metal promoted TiO_2 production of CO-free H_2, J. Phys. Chem. C. 116 (2012) 15396–15405.

[25] B. László, K. Baán, Z. Ferencz, G. Galbács, A. Oszkó, Z. Kónya, J. Kiss, A. Erdohelyi, Gold size effect in the thermal-induced reaction of CO_2 and H_2 on titania- and titanate nanotube supported gold catalysts, J. Nanosci. Nanotechnol. 19 (2019) 470–477.

[26] B. László, K. Baán, E. Varga, A. Oszkó, A. Erdohelyi, Z. Ferencz, Z. Kónya, J. Kiss, Photo-induced reactions in the CO_2-methane system on titanate nanotubes modified with Au and Rh nanoparticles, Appl. Catal. B 199 (2016) 473–484.

[27] J. Kiss, Á. Kukovecz, Z. Kónya, Beyond nanoparticles: The role of sub-nanosized metal species in heterogeneous catalysis, Catal. Lett. 149 (2019) 1441–1454.

[28] C. Marchal, T. Cottineau, M.G.M. Medrano, C.C. Justin, V. Caps, V. Keller, Au/ TiO_2–gC_3N_4 nanocomposites for enhanced photocatalytic H_2 production from water under visible light irradiation with very low quantities of sacrificial agents, Adv. Energy Mater. 8 (2018), 1702142.

[29] S. Zhu, S. Liang, Q. Gu, L. Xie, J. Wang, Z. Ding, P. Liu, Effect of Au supported TiO_2 with dominant exposed {0 0 1} facets on the visible-light photocatalytic activity, Appl. Catal. B 119 120 (2012) 146–155.

[30] Y. Fan, X. Yang, C.P. Yang, J.H. Liu, Au-TiO_2/graphene nanocomposite film for electrochemical sensing of hydrogen peroxide and NADH, Electroanalysis 24 (2012) 1334–1339.

[31] P. A. Stadelmann, JEMS - EMS java version (2004).

[32] W.F. Zhang, Y.L. He, M.S. Zhang, Z. Yin, Q. Chen, Raman scattering study on anatase TiO_2 nanocrystals, J. Phys. D: Appl. Phys. 33 (2000) 912–916.

[33] Y.Y. Wen, H.M. Ding, Y.K. Shan, Preparation and visible light photocatalytic activity of Ag/TiO_2/graphene nanocomposite, Nanoscale 3 (2011) 4411–4417.

[34] L.W. Zhang, H.B. Fu, Y.F. Zhu, Efficient TiO_2 photocatalysts from surface hybridization of TiO_2 particles with graphite-like carbon, Adv. Funct. Mater. 18 (2008) 2180–2189.

[35] X. Jiang, X.L. Li, X.F. Jia, G.Z. Li, X. Wang, G.Y. Wang, Z.S. Li, L.B. Yang, B. Zhao, Surface-enhanced Raman scattering from synergistic contribution of metal and semiconductor in TiO_2/MBA/Ag(Au) and Ag(Au)/MBA/TiO_2 assemblies, J. Phys. Chem. C. 116 (2012) 14650–14655.

[36] D. Tsukamoto, Y. Shiraishi, Y. Sugano, S. Ichikawa, S. Tanaka, T. Hirai, Gold nanoparticles located at the interface of anatase/rutile TiO_2 particles as active plasmonic photocatalysts for aerobic oxidation, J. Am. Chem. Soc. 134 (2012) 6309–6315.

[37] L. Tang, R. Ji, X. Li, K.S. Teng, S.P. Lau, Energy-level structure of nitrogen-doped graphene quantum dots, J. Mater. Chem. C. 1 (2013) 4908–4915.

[38] C. Zhang, L. Fu, N. Liu, M. Liu, Y. Wang, Z. Liu, Synthesis of nitrogen-doped graphene using embedded carbon and nitrogen sources, Adv. Mater. 23 (2011) 1020–1024.

[39] L.S. Panchakarla, K.S. Subrahmanyam, S.K. Saha, A. Govindaraj, H. R. Krishnamurthy, U.V. Waghmare, C.N.R. Rao, Synthesis, structure, and

properties of boron- and nitrogen-doped graphene, Adv. Mater. 21 (2009) 4726–4730.

[40] N. Roy, K. Bhunia, C. Terashima, A. Fujishima, D. Pradhan, Citrate-capped hybrid Au-TiO$_2$ nanomaterial for facile and enhanced electrochemical hydrazine oxidation, ACS Omega 2 (2017) 1215–1221.

[41] P. Lignier, M. Comotti, F. Schüth, J.-L. Rousset, V. Caps, Effect of the titania morphology on the Au/TiO$_2$-catalyzed aerobic epoxidation of stilbene, Catal. Today 141 (2009) 355–360.

[42] X. Lv, S.X. Zhou, C. Zhang, H.X. Chang, Y. Chen, W.-F. Fu, Synergetic effect of Cu and graphene as cocatalyst on TiO$_2$ for enhanced photocatalytic hydrogen evolution from solar water splitting, J. Mater. Chem. 22 (2012) 18542–18549.

[43] F. Wang, R.J. Wong, J.H. Ho, Y. Jiang, R. Amal, Sensitization of Pt/TiO$_2$ using plasmonic Au nanoparticles for hydrogen evolution under visible-light irradiation, ACS Appl. Mater. Interfaces 9 (2017) 30575–30582.

[44] J. Hou, H. Cheng, O. Takeda, H. Zhu, Three-dimensional bimetal-graphene-semiconductor coaxial nanowire arrays to harness charge flow for the photochemical reduction of carbon dioxide, Angew. Chem. Int. Ed. 54 (2015) 8480–8484.

[45] Y. Wang, J. Yu, W. Xiao, Q. Li, Microwave-assisted hydrothermal synthesis of graphene based Au-TiO$_2$ photocatalysts for efficient visible-light hydrogen production, J. Mater. Chem. A 2 (2014) 3847–3855.

[46] A. Ghosh, K.S. Subrahmanyam, K.S. Krishna, S. Datta, A. Govindaraj, S.K. Pati, C.N. R. Rao, Uptake of H$_2$ and CO$_2$ by graphene, J. Phys. Chem. C 112 (2008) 15704–15707.

[47] P.A. Bharad, K. Sivaranjani, C.S. Gopinath, A rational approach towards enhancing solar water splitting: a case study of Au-RGO/N-RGO-TiO$_2$, Nanoscale 7 (2015) 11206–11215.

[48] Y. Matsumoto, Energy positions of oxide semiconductors and photocatalysis with iron complex oxides, J. Solid State Chem. 126 (1996) 227–234.

[49] A. Ishikawa, T. Takata, J.N. Kondo, M. Hara, H. Kobayashi, K. Domen, Oxysulfide Sm$_2$Ti$_2$S$_2$O$_5$ as a stable photocatalyst for water oxidation and reduction under visible light irradiation ($\lambda \leq 650$ nm), J. Am. Chem. Soc. 124 (2002) 13547–13553.

[50] X. Li, W. He, C. Li, B. Song, S. Liu, Synergetic surface modulation of ZnO/Pt@ZIF-8 hybrid nanorods for enhanced photocatalytic CO$_2$ valorization, Appl. Catal. B 287 (2021), 119934.

[51] Q. Xu, J. Yu, J. Zhang, J. Zhang, G. Liu, Cubic anatase TiO$_2$ nanocrystals with enhanced photocatalytic CO$_2$ reduction activity, Chem. Commun. 51 (2015) 7950–7953.

[52] N. Sreekanth, M.A. Nazrulla, T.V. Vineesh, K. Sailaja, K.L. Phani, Metal-free boron-doped graphene for selective electroreduction of carbon dioxide to formic acid/formate, Chem. Commun. 51 (2015) 16061–16064.

[53] T.V. Vineesh, M.A. Nazrulla, K. Sailaja, T.N. Narayanan, S. Alwarappan, Synergistic effects of dopants on the spin density of catalytic active centres of N-doped fluorinated graphene for oxygen reduction reaction, Appl, Mater. Today 1 (2015) 74–79.

[54] J. Zhang, Z. Xia, L. Dai, Carbon-based electrocatalysts for advanced energy conversion and storage, Sci. Adv. 1 (2015), e1500564.

[55] X. Zou, M. Liu, J. Wu, P.M. Ajayan, J. Li, B. Liu, B.I. Yakobson, How Nitrogen-doped graphene quantum dots catalyze electroreduction of CO$_2$ to hydrocarbons and oxygenates, ACS Catal. 7 (2017) 6245–6250.

[56] Z.W. Seh, J. Kibsgaard, C.F. Dickens, I. Chorkendorff, J.K. Nørskov, T.F. Jaramillo, Combining theory and experiment in electrocatalysis: Insights into materials design, Science 355 (2017) eaad4998.

[57] K. Chan, J.K. Nørskov, Electrochemical barriers made simple, J. Phys. Chem. Lett. 6 (2015) 2663–2668.